∂ Observed Eddy–Internal Wave Interactions in the Southern Ocean

Jesse M. Cusack,[a] J. Alexander Brearley,[b] Alberto C. Naveira Garabato,[c]
David A. Smeed,[d] Kurt L. Polzin,[e] Nick Velzeboer,[f] and Callum J. Shakespeare[f]

[a] *Scripps Institution of Oceanography, University of California, San Diego, La Jolla, California*
[b] *British Antarctic Survey, Cambridge, United Kingdom*
[c] *University of Southampton, National Oceanography Centre, Southampton, United Kingdom*
[d] *National Oceanography Centre, Southampton, United Kingdom*
[e] *Woods Hole Oceanographic Institute, Woods Hole, Massachusetts*
[f] *Research School of Earth Sciences and ARC Centre of Excellence in Climate Extremes, Australian National University, Canberra, Australian Capital Territory, Australia*

ABSTRACT

The physical mechanisms that remove energy from the Southern Ocean's vigorous mesoscale eddy field are not well understood. One proposed mechanism is direct energy transfer to the internal wave field in the ocean interior, via eddy-induced straining and shearing of preexisting internal waves. The magnitude, vertical structure, and temporal variability of the rate of energy transfer between eddies and internal waves is quantified from a 14-month deployment of a mooring cluster in the Scotia Sea. Velocity and buoyancy observations are decomposed into wave and eddy components, and the energy transfer is estimated using the Reynolds-averaged energy equation. We find that eddies gain energy from the internal wave field at a rate of $-2.2 \pm 0.6 \, \mathrm{mW \, m^{-2}}$, integrated from the bottom to 566 m below the surface. This result can be decomposed into a positive (eddy to wave) component, equal to $0.2 \pm 0.1 \, \mathrm{mW \, m^{-2}}$, driven by horizontal straining of internal waves, and a negative (wave to eddy) component, equal to $-2.5 \pm 0.6 \, \mathrm{mW \, m^{-2}}$, driven by vertical shearing of the wave spectrum. Temporal variability of the transfer rate is much greater than the mean value. Close to topography, large energy transfers are associated with low-frequency buoyancy fluxes, the underpinning physics of which do not conform to linear wave dynamics and are thereby in need of further research. Our work suggests that eddy–internal wave interactions may play a significant role in the energy balance of the Southern Ocean mesoscale eddy and internal wave fields.

1. Introduction

The wind represents the largest energy source to the large-scale quasigeostrophic (QG) ocean circulation, providing 0.7–1 TW of work (Wunsch 1998; Scott and Xu 2009). More than 60% of this takes place in the Southern Ocean, where the time-mean wind work on the QG flow often exceeds $10 \, \mathrm{mW \, m^{-2}}$ locally (Hughes and Wilson 2008). Wind stress, in combination with atmospheric buoyancy forcing and dynamical instabilities, leads to the emergence of the Antarctic Circumpolar Current (ACC) and its vigorous mesoscale eddy field (Chelton et al. 2011). Mesoscale eddies play an important role in the Southern Ocean limb of the global overturning circulation by effecting isopycnal transports of mass and tracers across the ACC (Phillips and Rintoul 2000; Marshall and Speer 2012). They are also thought to facilitate diapycnal mixing in the abyss by driving deep currents that impinge on topography, with significant consequences for long-term climate (Sheen et al. 2014). Globally, mesoscale motions contain the majority of the ocean's kinetic energy (Ferrari and Wunsch 2009), yet it remains unclear how this energy is ultimately transferred to smaller-scale flows. The importance of resolving this issue is most evident in the Southern Ocean, where the rate and mechanisms of mesoscale eddy dampening may control the ACC transport and the depth of the global pycnocline (Marshall et al. 2017).

∂ Denotes content that is immediately available upon publication as open access.

Corresponding author: Jesse M. Cusack, jmcusack@ucsd.edu

Many boundary-focused mechanisms for dissipating mesoscale eddy energy and facilitating a forward cascade of energy toward smaller scales have been hypothesized, including (but not limited to) frictional drag at the bottom boundary (e.g., Arbic et al. 2009), lee wave generation (e.g., Nikurashin and Ferrari 2011), eddy scattering at western boundaries (e.g., Zhai et al. 2010), and submesoscale instabilities at the upper boundary (e.g., Molemaker et al. 2010; Zhang et al. 2016). Away from boundaries, it has been suggested that eddy–internal wave interactions could balance a significant fraction of the wind work in the ocean interior (Ferrari and Wunsch 2009). The relative importance of these mechanisms is not known, because they are not well constrained by the few observations that exist. For eddy–internal wave interactions in particular, previous observations were made in areas with modest eddy kinetic energy, and none in the Southern Ocean where the mechanism's potential for global influence is arguably largest (Marshall et al. 2017).

A diverse range of theoretical and observational studies illustrate how eddies and internal waves may interact. Theoretical analyses and ray tracing simulations indicate that vorticity associated with eddies alters the effective Coriolis frequency f_{eff} experienced by internal waves (Kunze 1985). Since propagating waves are dynamically constrained to locations where their frequency exceeds the effective Coriolis frequency, they may be trapped in areas where f_{eff} is locally small. Anticyclonic eddies may further facilitate the downward propagation and eventual dissipation of near-inertial waves via the "inertial chimney" effect (Lee and Niiler 1998; Zhang et al. 2018). Theoretical investigations suggest that waves may be captured by eddies if the local rate of eddy-induced strain exceeds the local relative vorticity (Jones 1969; Bühler and McIntyre 2005). If waves are captured, the strain may reduce their wavelength to the point of breaking. Waves may transfer momentum to eddy flows when they approach critical layers, where the wave phase speed is equal to the flow speed (Booker and Bretherton 1967). Eddies can also scatter internal waves (Dunphy and Lamb 2014), leading to the generation of higher modes that may be more susceptible to breaking. Recent work finds that internal wave-driven mixing appears to be modulated by the presence of mesoscale eddies over large regions of the ocean (Whalen et al. 2018). However, it remains to be determined which, if any, of the specific mechanisms outlined here play an important role.

One approach to the problem of eddy–internal wave interactions is to consider the propagation of waves through a QG eddy flow in the Wentzel–Kramers–Brillouin–Jeffreys (WKBJ) approximation limit (Müller 1976). In this framework, in which wavelength and time scales are assumed shorter than the scales of variation in the eddy flow quantities, individual waves conserve action density, which is equal to the wave energy density divided by the wave intrinsic frequency E/ω_0. The wave field as a whole can be represented by its action density spectrum, which may be perturbed by eddy straining as waves are stretched and squeezed (but not necessarily captured). A net transfer of energy from eddies to waves is achieved by nonlinear processes within the wave field, such as triad interactions (Olbers 1976), acting to relax the action spectrum to some background state. This treatment suggested that the impact of internal waves was to damp eddy motions, and that the effect could be parameterized by horizontal and vertical viscosity coefficients, $\nu_h = 7 \, \mathrm{m^2 \, s^{-1}}$ and $\nu_v = 0.4 \, \mathrm{m^2 \, s^{-1}}$, respectively, acting on momentum but not passive tracers (Müller 1976).

Early in situ observational investigation of this type of interaction was undertaken using data from several mooring arrays in the western North Atlantic, including the Mid Ocean Dynamics Experiment (MODE) (Frankignoul 1976), the Internal Wave Experiment (IWEX) (Frankignoul and Joyce 1979), PolyMode arrays I and II (Ruddick and Joyce 1979), and the PolyMode Local Dynamics Experiment (LDE) (Brown and Owens 1981). All of these works failed to produce an estimate of the vertical viscosity that was statistically different from zero. A reanalysis of the LDE data (Polzin 2010) produced estimates of the horizontal viscosity, $\sim 50 \, \mathrm{m^2 \, s^{-1}}$, and an effective vertical viscosity of $(2.5 \pm 0.3) \times 10^{-3} \, \mathrm{m^2 \, s^{-1}}$. To summarize this body of previous observational work, the vertical viscosity of wave–eddy interactions is likely to be several orders of magnitude smaller than the theoretical estimate of Müller (1976), whereas the horizontal viscosity could be an order of magnitude larger.

In this paper, the strength of the interaction between eddies and internal waves is quantified through an analysis of the transfer terms in the internal wave energy equation. The technique remains indifferent to the details of the mechanism controlling the interaction, so long as the approximations that underpin the equation are valid. The transfer terms are as follows:

$$F_h = -\frac{1}{2}\overbrace{(\overline{u'u'} - \overline{v'v'})}^{\text{normal stress}} \overbrace{\left(\frac{\partial \overline{u}}{\partial x} - \frac{\partial \overline{v}}{\partial y}\right)}^{\text{normal strain rate}} - \underbrace{\overline{u'v'}}_{\text{shear stress}} \overbrace{\left(\frac{\partial \overline{v}}{\partial x} + \frac{\partial \overline{u}}{\partial y}\right)}^{\text{shear strain rate}},$$

(1)

$$F_v = -\overbrace{(\overline{u'w'} - fN^{-2}\overline{b'v'}, \overline{v'w'} + fN^{-2}\overline{b'u'})}^{\text{EP flux vector}} \cdot \overbrace{\left(\frac{\partial \overline{u}}{\partial z}, \frac{\partial \overline{v}}{\partial z}\right)}^{\text{shear vector}},$$

(2)

where F_h and F_v represent horizontal and vertical energy transfers, respectively. Standard notation is used such that

(u, v, w) represent zonal, meridional, and vertical velocity in the (x, y, z) directions. Additionally, b is buoyancy, and f and N denote the Coriolis and buoyancy frequencies, respectively. Eddy quantities are indicated by an overline ($\overline{u}$) and internal wave quantities by primes (u'). The two scales are separated using a temporal filter, which is explained further in section 2. The horizontal energy transfer is facilitated by straining of internal waves by eddies. The vertical energy transfer is facilitated by vertical shearing of waves by eddies. The vertical stress is equivalent to the Eliassen–Palm (EP) flux and includes contributions from the horizontal buoyancy flux (Eliassen and Palm 1961). The key approximations used in the derivation are those of QG eddy dynamics and linear internal wave dynamics. A more detailed explanation of the origin of these equations can be found in Müller (1976). The relation between the equations and the viscosity parameters presented in previous publications is elaborated upon in appendix A.

A positive transfer of energy from eddies to waves does not necessarily involve generation of waves, but can also represent an amplification of the existing field. Shakespeare and Hogg (2017) diagnose such a positive transfer in a numerical model, in which waves generated through submesoscale instabilities at the surface propagate downward and are amplified in the interior by interaction with eddies. Rocha et al. (2018) demonstrate that straining of near-inertial waves by barotropic eddies is a significant sink of eddy kinetic energy in an idealized simulation. Polzin (2010) reports a net energy transfer from eddies to waves on the order of $4 \times 10^{-10}\,\mathrm{W\,kg^{-1}}$ at a depth of 600–825 m from observations in the Northwest Atlantic. Jing et al. (2018) estimate an energy transfer on the order of $5 \times 10^{-11}\,\mathrm{W\,kg^{-1}}$ between depths of 250 and 500 m from observations in the Gulf of Mexico; however, they estimate only the energy exchange due to horizontal stresses, neglecting the vertical component. A key finding of our paper is that the vertical component of the energy transfer rate should not be neglected, because it may be larger in magnitude than the horizontal component and of opposite sign.

Our goal in this paper is to present quantitative estimates of energy transfers between eddies and internal waves in an area of the Southern Ocean known for being both a mesoscale eddy hotspot and a prominent internal wave generation site. Section 2 details the data sources and analysis methods. Section 3 presents the energy transfer estimates, which are discussed further in section 4. Conclusions are provided in section 5.

2. Methodology

The data and code used to conduct the analysis in this paper are available online (Cusack 2020; https://doi.org/10.5281/zenodo.3924818).

a. Data sources

1) MOORING ARRAY

The observations presented in this paper stem primarily from a mooring array located upon a 3700-m-deep seamount in the Scotia Sea (Brearley et al. 2013; Sévellec et al. 2015), close to the climatological position of the Subantarctic Front (SAF) (Fig. 1a). The array was one component of the Diapycnal and Isopycnal Mixing Experiment in the Southern Ocean (DIMES). It was deployed from the RRS *James Cook* on 9–11 December 2009, recovered on 6–7 December 2010, redeployed on 18–20 December 2010, and finally recovered on 5–6 March 2012. The array configuration, displayed in Fig. 1b, consisted of five moorings arranged in a cross. A sixth mooring was deployed but suffered from multiple instrument failures that preclude its use in this paper. We denote individual moorings by their cardinal position in the array, for example, NW refers to the northwest mooring while C denotes the central mooring.

Failure of the SW and NE moorings during the first deployment period reduced the array to a diagonal line, greatly hindering the array's resolution of lateral velocity structure. Consequently, data from this period is not presented in this paper. The second deployment period provided 437 days (42 048 samples) of continuous data from all instruments, except for one Seaguard current meter located on the SW mooring, which experienced a premature battery failure and provided 146 days of data. All moorings were instrumented with Nortek acoustic current meters, Seaguard acoustic current meters and Seabird Electronics SBE37 Microcat CTDs. Details of the instrumentation are provided in Table 1 and simple mooring diagrams are plotted in Fig. 1c. The outer moorings were instrumented with 5 pairs of CTDs and current meters, while the C mooring had 12. The C mooring was also instrumented with a downward-looking Teledyne Marine workhorse long-ranger ADCP.

2) MICROSTRUCTURE DATA

Measurements of the turbulent kinetic dissipation rate ε were obtained with two Rockland Scientific VMP-5500 free-fall vertical microstructure profilers during the same cruise that recovered and redeployed the moorings. Details of data processing are available in Sheen et al. (2013). In total, 15 VMP profiles were conducted between 8 and 23 December 2010 in the vicinity of the mooring array. Their location relative to the moorings is displayed in Fig. 1b.

b. Mooring motion correction

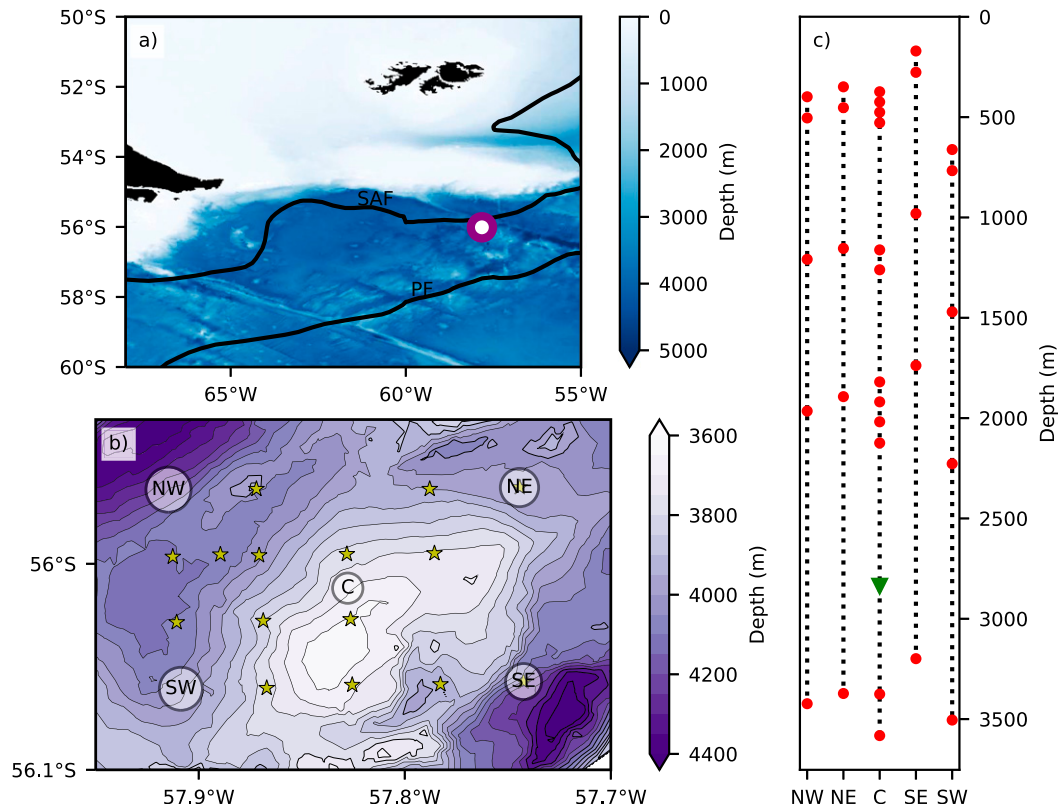Strong upper-ocean horizontal flow caused significant mooring knock-down, on occasion by as much

FIG. 1. (a) Regional map of seafloor topography, with mooring array location marked by a purple circle. Black lines show the climatological position of the Polar and Subantarctic Fronts (Orsi et al. 1995). (b) Mooring positions, with high-resolution multibeam topography contoured in 50-m intervals. Vertical microstructure stations are denoted by yellow stars. (c) Simple mooring diagrams, where red circles indicate the positions of current meter–CTD pairs, and the green triangle indicates a downward looking long-ranger ADCP.

as 800 m for the shallowest instruments. Observations were interpolated to fixed height levels z_i using a method similar to that reported in Brearley et al. (2013), which was based on the work of Hogg (1986, 1991) and Cronin et al. (1992). In summary, canonical profiles q_c (e.g., velocity or density) were estimated by fitting polynomials to all available mooring data as a function of height. These profiles provide an estimate of the time-mean vertical structure of the data. At any given mooring, there exist two instruments closest to a specific fixed level at heights z_1 and z_2. The values measured by these instruments are denoted $q(z_1)$ and $q(z_2)$. The interpolated value is then given by the following equation:

TABLE 1. Mooring location, bottom depth H, minimum instrument depths, and sampling intervals T_S. Each current meter was paired with an SBE SB37 MicroCAT with the same sampling interval.

| Mooring	Longitude	Latitude	H (m)	Instrument	Depth (m)	T_S (min)
C	57°49.66′W	56°0.71′S	3672	Nortek	373, 424, 476, 528	15
				Nortek	1162, 1261, 1819, 1919	15
				Nortek	2018, 2124, 3375, 3582	15
				Long-ranger ADCP	2836–3396	30
NW	57°54.88′W	55°57.84′S	4113	Seaguard	398, 504, 1965, 3423	15
				Nortek	1209	15
SW	57°54.52′W	56°3.64′S	3965	Seaguard	661, 767, 1470, 3505	15
				Nortek	2227	15
SE	57°44.54′W	56°3.43′S	3949	Seaguard	170, 276, 981, 1738	15
				Nortek	3199	15
NE	57°44.66′W	55°57.78′S	4902	Seaguard	349, 453, 1154	15
				Nortek	1893, 3372	15
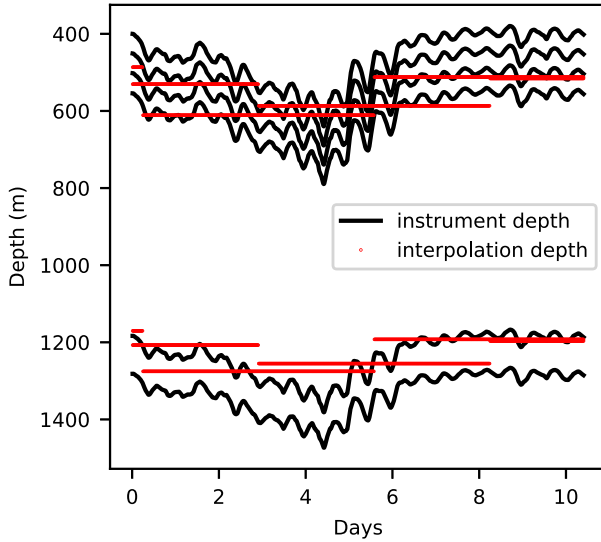
FIG. 2. An example of instrument depths and interpolation depths for the upper portion of C mooring for a 10-day segment of data. The interpolation depths vary to account for knock-down, and the interpolated segments overlap in time by 50%.

$$q(z_i) = w_1[q_c(z_i) - q_c(z_1) + q(z_1)] + w_2[q_c(z_i) - q_c(z_2) + q(z_2)], \tag{3}$$

where the weighting functions w_1 and w_2 are related by

$$w_2 = 1 - w_1 = \frac{|z_i - z_2|}{|z_i - z_2| + |z_i - z_1|}. \tag{4}$$

The quantities interpolated with this method were neutral density, using a third-order polynomial, and zonal and meridional velocities, using second-order polynomials. The method is effective at suppressing spurious values that can be caused by linear extrapolation. The interpolation height was varied to account for mooring knock-down, with the goal of keeping z_i close to groups of instruments at the C mooring (Fig. 2). A consequence of the variable interpolation height is that estimates of the energy transfer rates presented in this paper should be interpreted as averages over a range of depths. The mean depths at which we estimate the transfers are 566, 1243, 2084, and 3388 m.

Since instrument depths do not necessarily line up perfectly across moorings (Fig. 1c), larger interpolation distances were necessary at the outer moorings. The error associated with interpolation is investigated using a numerical model in appendix B. Only the eddy velocities ($\overline{u}$, $\overline{v}$) were estimated at the outer moorings. The vertical velocity w', buoyancy perturbation b', and density gradient $\partial \rho / \partial z$, as well as the full horizontal velocity (u, v), were only calculated at the more heavily instrumented C mooring.

c. Definition of eddy and internal wave quantities

The separation of internal wave and eddy quantities was achieved by a combination of moving window averages and Fourier transform methods. The corrected time series were first divided into 512 data point (~5 day) windows that overlap by 256 points. The window length was chosen pragmatically to be long enough to contain several inertial periods, and enough data points to provide reliable statistics, but not so long as to smooth over eddy time scales. Internal waves were defined as motions with a frequency between f and N within a given window. At the latitude of the mooring array, $2\pi/f \approx 14$ h and $2\pi/N \approx 0.8$–1.9 h. Eddy quantities were estimated by applying a mean weighted by a Hanning function to each window.

Internal wave vertical velocity w' was not measured directly and was calculated from the internal wave density perturbation using

$$w' = -\frac{\partial \rho'}{\partial t}\left(\frac{\partial \overline{\rho}}{\partial z}\right)^{-1}, \tag{5}$$

where ρ denotes density. Neutral density was used as the density variable (Jackett and McDougall 1997). Estimating vertical velocity in this way assumes that advection of internal-wave-induced horizontal density gradients by the mesoscale flow makes a negligible contribution to w'. This important assumption is discussed in appendix B. Interpolation of quantities to fixed levels ensures that there is no correlation between w' and the vertical motion of the mooring (quantified as the rate of change in instrument depth). Other quantities used throughout this paper include internal wave buoyancy perturbation, $b' = -g(\rho'/\overline{\rho})$. Buoyancy frequency N is calculated from temperature, salinity, and pressure using the EOS-80 thermodynamic toolbox.

d. Calculating internal wave stresses

At each window, the cross spectra $X(\omega)$ of the buoyancy and velocity components were calculated. A Hanning window was applied to reduce spectral leakage. The wave stress components were computed by integrating the real part of the cross spectrum, also known as the cospectrum [denoted $C(\omega)$], between f and N. For example, the shear stress was calculated as follows:

$$\overline{u'v'} = \int_f^N C_{uv}(\omega)\, d\omega. \tag{6}$$

The vertical stress terms were estimated directly from the density perturbation, i.e.,

$$\overline{u'w'} = -\left(\frac{\partial \overline{\rho}}{\partial z}\right)^{-1} \int_f^N \mathrm{Re}[i\omega X_{u\rho}(\omega)]\, d\omega, \qquad (7)$$

with an equivalent expression for $\overline{v'w'}$. This result follows from the mathematical properties of Fourier transforms applied to derivatives, i.e., $F(\partial \rho'/\partial t) = i\omega F(\rho')$. The advantage of working directly with density perturbation in frequency space is that no finite difference methods need be applied to estimate w'.

e. Calculating eddy velocity gradients

Stokes' theorem applied to a two-dimensional plane, also known as Green's theorem, provides a framework for estimating horizontal gradients of quantities at the mooring array (Bryden and Fofonoff 1977). When applied to velocity, this theorem relates the vorticity integrated over an area A to the integral of the velocity tangent to the line enclosing the area. Assuming that vorticity is constant over the area in question, the following simplified equation can be derived:

$$\frac{\partial \overline{v}}{\partial x} - \frac{\partial \overline{u}}{\partial y} = \frac{1}{A} \oint \overline{\mathbf{u}} \cdot d\mathbf{s}, \qquad (8)$$

where $d\mathbf{s}$ is an infinitesimal line element. An analogous two-dimensional application of the divergence theorem relates the horizontal divergence to the line integral of the velocity normal to the enclosing line. Individual velocity gradients are related to line integrals of individual velocity components, for example,

$$\frac{\partial \overline{u}}{\partial x} = \frac{1}{A} \oint \overline{u} n_x \, dx, \qquad (9)$$

where n_x is the x component of the unit vector that points normal to the line. Similar expressions exist for the other horizontal derivatives. At the DIMES mooring array, the line integrals are calculated around the outer four moorings (Fig. 1b). The numerical approximation to the exact integral uses the velocity averaged between pairs of moorings, and takes the line elements as the distances between the moorings. An advantage of the method over finite differencing is that it is easy to handle arrays of arbitrary shape.

The vertical shear in horizontal velocity ($\partial \overline{u}/\partial z$, $\partial \overline{v}/\partial z$) was estimated using finite-differencing methods at the C mooring. The vertical spacing of the instruments varied from 50 m for the upper four instruments, to 100 m at middepth, and 200 m near the bottom. Thus, the resolution is greatest near the surface. Eddy shear was estimated as the depth average over closely spaced instruments.
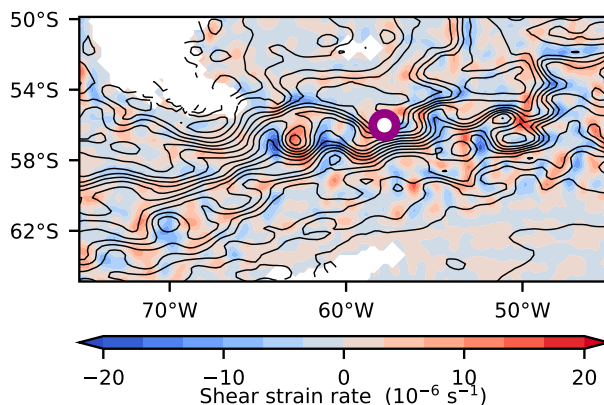

FIG. 3. An illustrative snapshot of shear strain rate colored over a region containing the mooring array, which is denoted by a purple circle. Absolute dynamic topography is contoured in increments of 0.1 m. Strain rate and dynamic topography were derived from the 1/4° AVISO all sat merged dataset.

Consequently, the effective vertical scale of the shear calculation varied between 100 and 500 m, depending on the cluster of instruments used.

f. Summary of errors

Errors in our estimates of the energy transfer rate arise from several sources and extensive details are provided in appendix B. The most significant source of error results from the interpolation of sparse observations to fixed depth levels. In particular, the estimates of horizontal eddy gradients near the surface and vertical shear near the bottom are likely to be noisy. The next most significant source of error results from a combination of interpolation error and instrumental noise in the estimates of internal wave vertical stresses, and is likely highest near the surface. The impact of Doppler shifting on our wave stress estimates is unknown, but suspicious trends between eddy flow speed and stress are not present. All quantifiable sources of error are assumed independent and propagated to the final results using standard methods (Taylor 1997).

3. Results

a. Mesoscale eddy flow

The dominant features of the mesoscale flow are the jets and eddies associated with the Antarctic Circumpolar Current (ACC). Figure 3 depicts the surface geostrophic flow on 25 March 2011 in the Scotia Sea, using absolute dynamic topography as a proxy for a streamfunction. Eddies are generated upstream of the Drake Passage, intensify as they enter the passage, and then transit past the mooring array. The strong flow of the ACC forces the typically westward-propagating eddies to move eastward. The accompanying rate of strain field is also displayed.
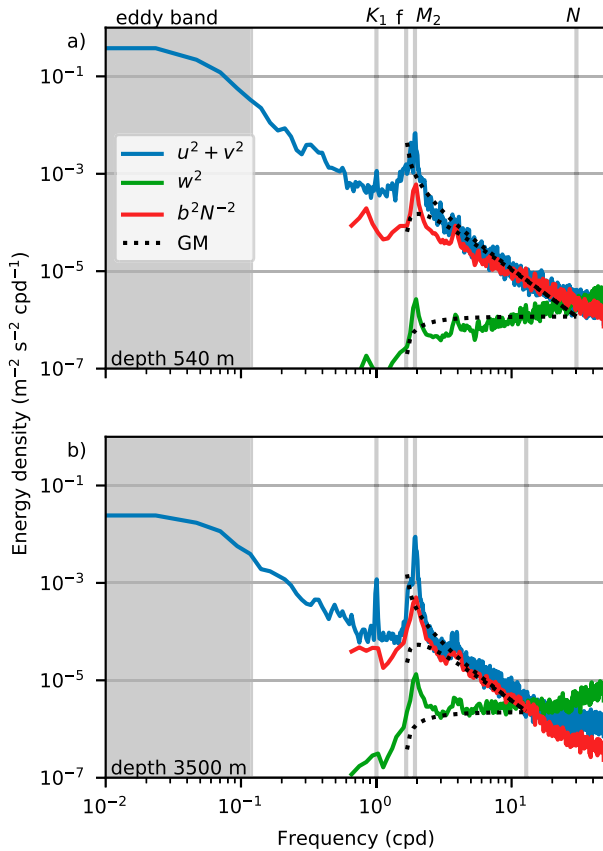
FIG. 4. Spectra from C mooring at depths of (a) 540 and (b) 3500 m of horizontal kinetic energy ($u^2 + v^2$), potential energy ($b^2 N^{-2}$), and vertical kinetic energy (w^2). Garrett–Munk spectra are added as dashed lines, using the formulation described by Cairns and Williams (1976). Solid vertical lines indicate the K_1 and M_2 tidal constituents, the Coriolis frequency f, and the buoyancy frequency N. The shaded region on the left denotes the eddy portion of the spectrum, which corresponds to periods longer than about 5 days, set by the averaging period used in the analysis.

Strong straining regions generally occur at kinks and bends in the path of ACC jets or in the confluence of eddy flow structures.

Important time scales of variability in the flow may be diagnosed from spectra of horizontal kinetic energy, presented in Fig. 4. The eddy velocity band encompasses motions occurring over periods greater than 5 days, with energy density plateauing at the longest resolved periods. Normal and shear strain rate spectra also plateau in the same band (not shown). Eddy kinetic energy declines by approximately an order of magnitude from the surface to near the bottom, indicating that the strongest eddy motions are confined to the upper ocean.

b. Internal wave field

The slopes of potential, horizontal kinetic and vertical kinetic energy spectra in the internal wave frequency band are generally consistent with the canonical Garrett–Munk (GM) spectrum between f and N (Fig. 4) (Cairns and Williams 1976). There are significant peaks in the spectra at the inertial frequency, M_2 tidal frequency, and harmonics of the semidiurnal tides. A peak is also observed at the K_1 frequency, although this is subinertial. Global tidal inversion models suggest that the barotropic components of M_2 and S_2 have an amplitude of about $1 \, \mathrm{cm \, s^{-1}}$ in this area (Egbert and Erofeeva 2002). However, the peaks in potential and vertical kinetic energy indicate the presence of internal tides, which are not represented in the GM spectra. The energy in the internal wave band remains relatively constant with depth, although the bandwidth decreases because the stratification weakens with depth.

c. Horizontal energy transfer rate

Time series of energy transfer rate from eddies to waves due to horizontal straining of the internal wave field are calculated for various depth ranges (Fig. 5). The time series reveal large variability in the sign and magnitude of the transfer. The magnitude of the mean transfer rate at 566 m is $(3 \pm 2) \times 10^{-10} \, \mathrm{W \, kg^{-1}}$ (Fig. 5e). The quoted error denotes the 95% confidence interval. Below 1000 m, the magnitude of the transfer rate is small, and close to the bottom it becomes negative, indicating a transfer from waves to eddies.

Cumulative integrals of horizontal energy transfer in frequency space provide a way of assessing which frequency band contributes most to the transfer rate (Fig. 6). At 566 m, low frequencies ($<2f$, including semidiurnal tides) contribute roughly half of the final transfer rate. Close to the bottom, near inertial frequencies are responsible for all of the energy transfer. In the middepth range no particular frequency band dominates.

Time series of horizontal energy transfer rate indicate that the transfer takes place in frequent short events (Fig. 5). Two such events were observed at 566-m depth and are found to be associated with large near-inertial fluctuations in velocity (Fig. 7a) and peaks in the shear stress (Fig. 7c). The shear strain and stress (Figs. 7b,c) are coherent during this period. The normal strain and stress remain relatively low in comparison. Consequently, the total energy transfer rate (Fig. 7d) is dominated by the shear contribution. At the shallowest instrument level, the shear terms are responsible for the vast majority of the energy transfer ($\sim$90%). Below 2000-m depth, the shear and normal terms are approximately equal in magnitude but opposite in sign.

d. Vertical energy transfer rate

Time series of the energy transfer rate from eddies to waves due to vertical shearing of the internal wave field
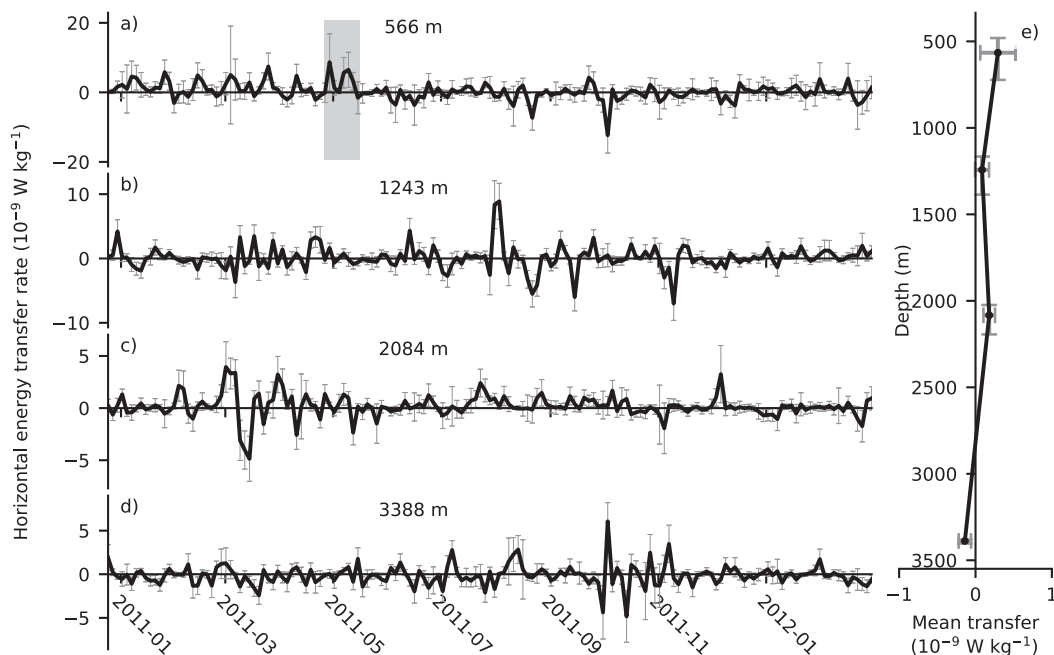
FIG. 5. Time series of horizontal energy transfer rate from (a) 566, (b) 1243, (c) 2084, and (d) 3388 m, as well as (e) the time-mean transfer rate. Error bars represent the 95% confidence interval. The shaded region in (a) is expanded in Fig. 7.

are calculated for several depth ranges (Fig. 8). As with the horizontal transfer, the time series reveal large variability in the sign and magnitude of the vertical transfer rate. Following Ruddick and Joyce (1979), we estimate the vertical transfer in two ways. The first, referred to as the "full" transfer, is given by Eq. (2). The second, referred to as the "effective" transfer, is given by the following approximation:

$$F_v \approx -\left(1 - \frac{f^2}{\omega^2}\right)(\overline{u'w'},\ \overline{v'w'}) \cdot \left(\frac{\partial \overline{u}}{\partial z}, \frac{\partial \overline{v}}{\partial z}\right). \qquad (10)$$

The reason for using this approximation is to enforce the result from linear internal wave theory that buoyancy flux terms cancel vertical stress terms at the inertial frequency. This is equivalent to stating that near-inertial waves should play a negligible role in the vertical energy transfer. Furthermore, the buoyancy flux contribution from higher-frequency waves should also be negligible.

We find that the full and effective stresses provide similar estimates of the net vertical energy transfer in the upper 2000 m of the water column (Fig. 8e). The magnitude of the full vertical transfer rate at 566 m is $(-10 \pm 5) \times 10^{-10}\,\mathrm{W\,kg^{-1}}$, comparable to an effective transfer rate of $(-8 \pm 5) \times 10^{-10}\,\mathrm{W\,kg^{-1}}$. This suggests that there is a relatively strong cancellation of buoyancy fluxes and vertical stresses in the upper ocean, consistent with linear internal wave dynamics. However, the

buoyancy terms do increase the magnitude of the transfer slightly when included. The sign of the flux is negative, implying an energy transfer from waves to eddies. Near the bottom, the two estimates diverge significantly, implying that there is a strong contribution to the flux from the buoyancy terms. A lack of
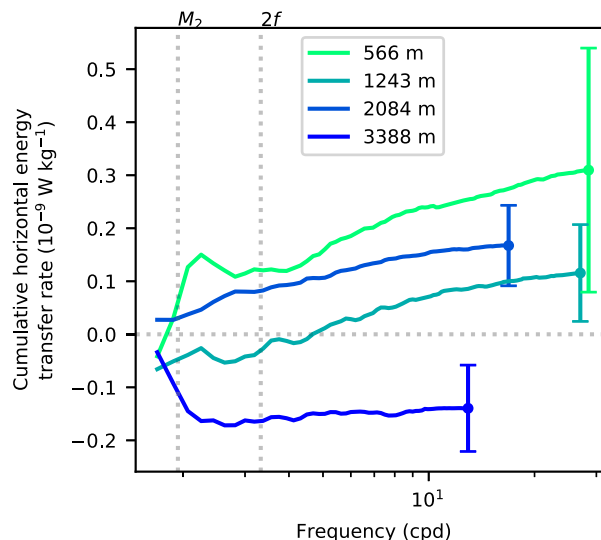

FIG. 6. Cumulative sums of the horizontal energy transfer rate in frequency for each depth level. The error bars denote the 95% confidence interval on the final point.
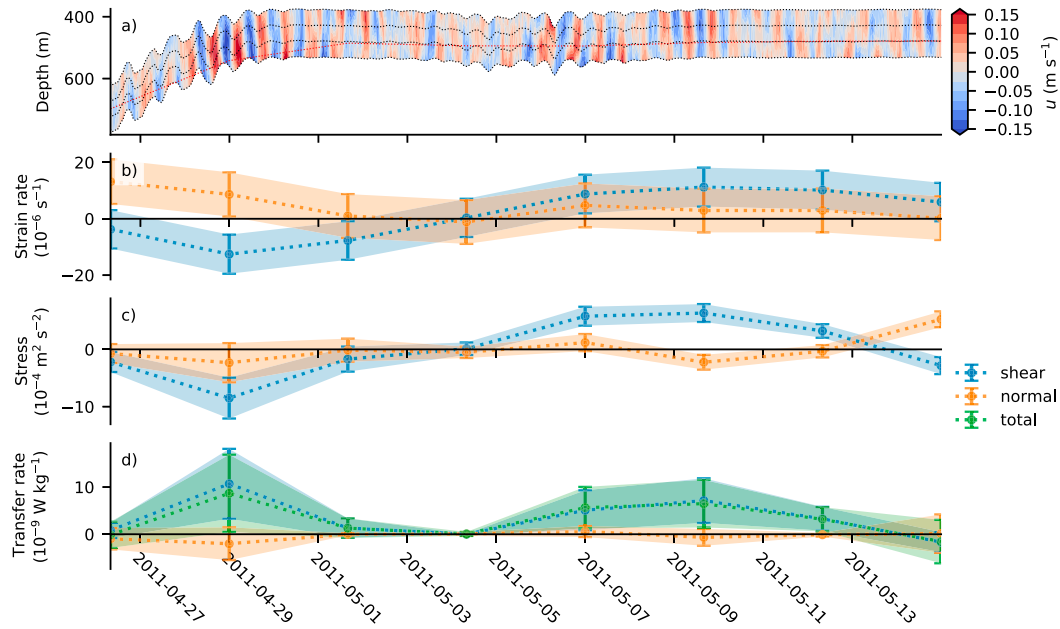
FIG. 7. Time series of (a) high-pass-filtered zonal velocity from the four uppermost current meters. The thin black dashed lines mark the positions of the instruments. The thin dashed red line indicates the level at which the stress, strain, and transfers are estimated. Time series of (b) normal and shear strain rates, (c) normal and shear stresses, and (d) energy transfer, including contributions from normal and shear terms separately.

cancellation also implies that assumptions of linear internal wave dynamics do not hold near topography.

Vertical energy transfers are greater in magnitude than horizontal energy transfers. However, the root-mean-square (RMS) vertical stress is about $2 \times 10^{-5} \mathrm{m^2 s^{-1}}$, an order of magnitude less than the RMS horizontal shear stress of $3 \times 10^{-4} \mathrm{m^2 s^{-1}}$. At the shallowest instruments, RMS vertical shear is $\sim 1 \times 10^{-4} \mathrm{s^{-1}}$, compared to an RMS horizontal shear strain rate of $\sim 7 \times 10^{-6} \mathrm{s^{-1}}$. Thus, vertical shear is typically more than an order of magnitude greater than the horizontal strain rate. As such, we conclude that the strong vertical shears associated with mesoscale features of the ACC are essential in mediating the energy transfer.

A little less than half of the vertical energy transfer rate diagnosed at the upper two levels is effected at semidiurnal frequencies (Fig. 9), with the rest distributed over higher frequencies. At the deepest level, semidiurnal and near-inertial frequencies facilitate a positive transfer, which is more than offset by a large negative transfer due to higher frequencies. At 2084 m, the vertical energy transfer rate is negligible at all frequencies.

Near-bottom buoyancy fluxes that lead to large negative energy transfers occur in short events. Two such events took place over the course of a few days in August 2011 (Fig. 10). The peaks in vertical transfer are concurrent with large fluctuations in buoyancy and

velocity (Figs. 10b,c). Velocity phase lines are slanted downward (Fig. 10a), indicating that the dominant mode is upward propagating. The frequency of the fluctuations is close to the inertial and M_2 frequencies. The effective transfer rate has a smaller magnitude than the full transfer rate (Fig. 10d). This event illustrates that large, near-bottom energy transfers are associated with relatively low-frequency fluctuations in buoyancy and velocity. However, frequency space analysis (Fig. 9) reminds us that it is actually the less visually obvious, higher frequencies, that are ultimately responsible for the negative sign of the transfer.

e. Anisotropy in the internal wave field

The direction of the EP flux plays an important role in setting the magnitude of the vertical energy transfer, because it appears in Eq. (2) as a vector product with the shear vector. Physically, the EP flux represents a combination of internal wave-mediated vertical fluxes of horizontal momentum and horizontal fluxes of buoyancy. The magnitude and direction of the EP flux are determined by the amplitude and direction of propagation of the internal waves that comprise the internal wave field. For a single plane wave, the EP flux is oriented along the horizontal axis of wave propagation, although its sign may vary depending on the vertical direction of propagation. At the shallowest instruments, the EP flux vector does not have a strongly preferred
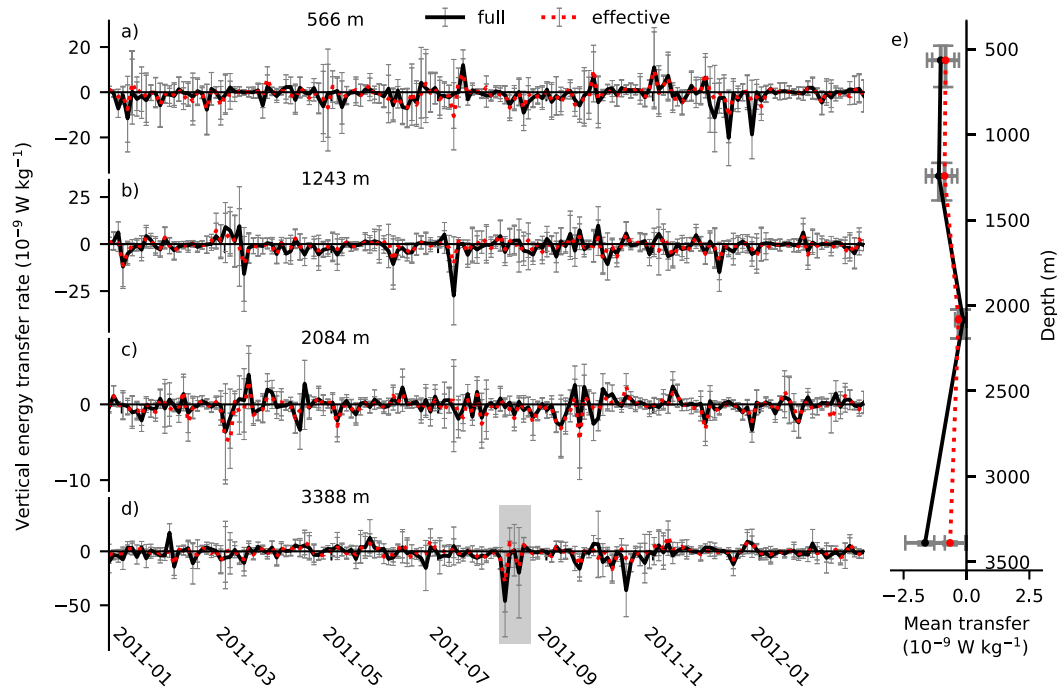
FIG. 8. Time series of vertical energy transfer rate from (a) 566, (b) 1243, (c) 2084, and (d) 3388 m, including the effective approximation (red dashed), as well as (e) the time-mean transfer rate. Error bars represent the 95% confidence interval. The shaded region in (e) is expanded in Fig. 10.

orientation (Fig. 11a), indicating that the internal wave field is somewhat isotropic. At the deepest instrument level, however, the EP flux is oriented toward the southeast (Fig. 11b), implying that the internal wave field is composed largely of waves propagating along the northwest–southeast axis.

The azimuthal axis of wave propagation as a function of frequency, $\theta = \theta(\omega)$, can also be estimated from cospectra of velocity using the following equation (Gonella 1972),

$$\tan(2\theta) = \frac{2C_{uv}}{C_{uu} - C_{vv}}. \tag{11}$$

It should be noted that waves with horizontal wave-vector (k, l) and $(-k, -l)$ would be determined to have the same azimuthal angle, despite propagating in opposite directions. That is why we refer to θ as the azimuthal axis (e.g., east–west corresponds to 0°) rather than the azimuthal angle. 2D histograms were constructed by binning θ estimates at each sequential window in the time series, for two different depths, into θ–ω space. An isotropic wavefield would contain an equal number of counts n_i in each bin. We define the deviation from an isotropic wavefield as $(n - n_i)/n_i$. To account for instrument noise, significance is assessed relative to a white noise background with a standard

deviation of 1 cm s^{-1}. At the shallowest instrument level, there is little indication that waves of any frequency have a preferred horizontal axis of propagation (Fig. 11c). At the deepest level, there is a clear preference for propagation along the southeast axis at all
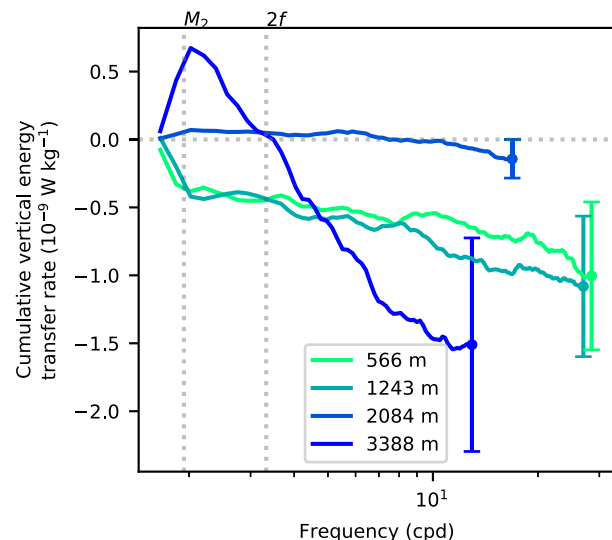

FIG. 9. Cumulative sums of the vertical energy transfer rate in frequency for each depth level. The error bars denote the 95% confidence interval on the final point.
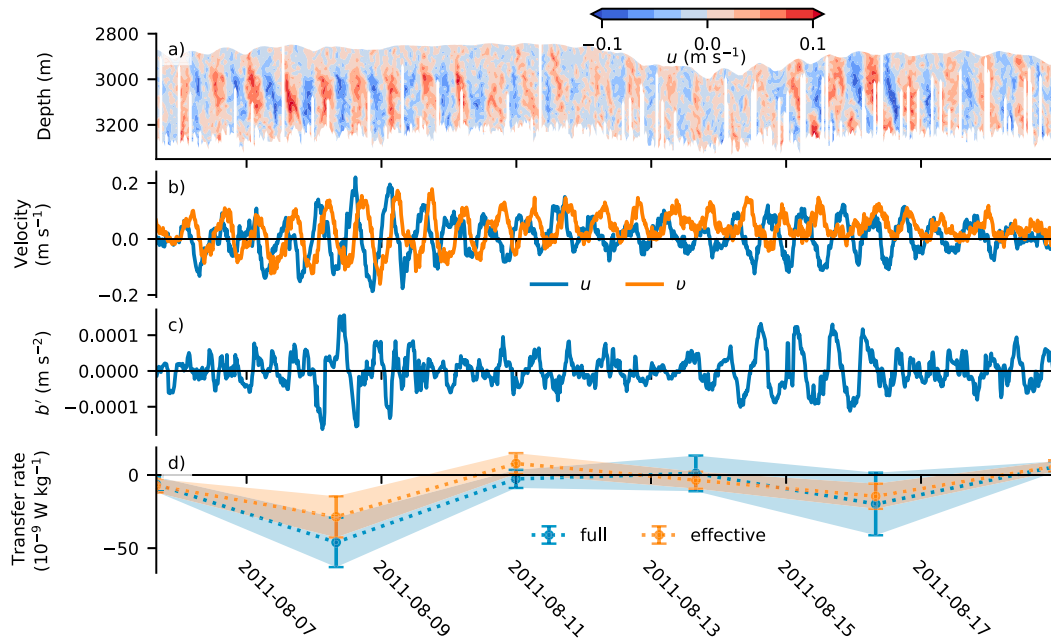
FIG. 10. Time series of (a) high-pass zonal velocity from the downward-looking long-ranger ADCP, (b) zonal and meridional velocity from the deepest current meter, (c) buoyancy, and (d) the full and effective vertical energy transfer rates.

frequencies (Fig. 11d), which is consistent with the direction of the EP flux. The seamount upon which the observations were made (Fig. 1b) is approximately elliptical, with the minor axis orientated northwest to southeast. We speculate that the anisotropy in internal wave field arises, in part, from wave generation processes at an anisotropic topographic feature. The central mooring is not located exactly on top of the seamount, and this may lead to spatial aliasing of the observations.

f. Toward an energy budget

The horizontal and vertical transfers can be combined into a total energy transfer estimate (Fig. 12). The total transfer is dominated by the vertical component and is generally negative, implying a net transfer of energy from waves to eddies. The magnitude of the total transfer at 566 m is $(-7 \pm 6) \times 10^{-10}$ W kg^{-1}. Cumulative integrals of the transfer (Figs. 12a–d) illustrate how energy is mostly transferred in steps, associated with the short events discussed previously, rather than as a gradual accumulation. This is especially true near the bottom, where a few large steps account for the majority of the energy transferred.

The depth-integrated transfer rate can be compared with the contributions from other physical mechanisms known to dissipate eddy and internal wave energy. To facilitate comparison, horizontal, vertical, and total energy transfers are depth-integrated between 3388 and 566 m, and multiplied by a constant density, $\rho_0 = 1025$ kg m^{-3}, to

generate an energy flux in units of watts per square meter. Turbulent dissipation rates from VMP profiles are averaged and integrated over the same depth range as the eddy–internal wave energy transfers. The dissipation rate in the bottom boundary layer is estimated from a simple drag parameterization (Taylor 1920),

$$F_{\mathrm{BBL}} = \rho_0 C_d U^3, \qquad (12)$$

where the drag coefficient is pragmatically taken to be $C_d = 2 \times 10^{-3}$, and U is the RMS speed of the total flow (wave plus eddy) from the deepest current meter at mooring C, located approximately 100 m above the bottom. We note that there is a considerable range in plausible values for the drag coefficient, which could be as large as 7.5×10^{-3} (e.g., Trowbridge and Lentz 1998). Finally, an estimate of the energy flux into the internal wave field via lee wave generation is taken directly from Brearley et al. (2013). This estimate is made by an application of linear lee wave generation theory (Bell 1975) combined with observational estimates of the bottom flow speed, stratification, and topographic spectrum from the first mooring deployment period.

Broadly, energy transfers fall into two categories: 1) transfers of energy between eddies and internal waves, and 2) dissipation of total (wave plus eddy) kinetic energy (Fig. 13). The integrated horizontal energy transfer is negligibly small when compared to the other processes. The integrated vertical energy transfer is
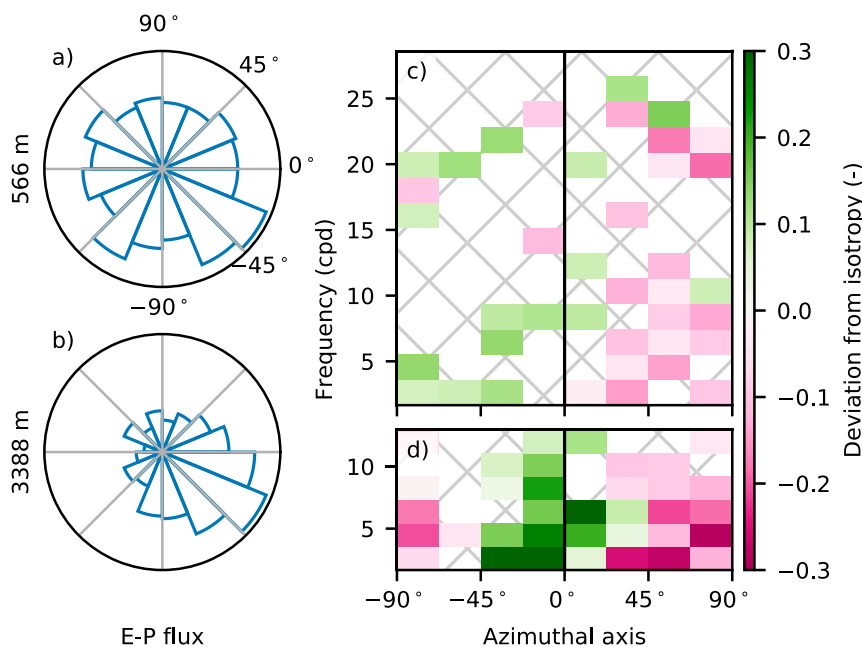
FIG. 11. (a), (b) Polar histograms of the EP flux vector. The number of points in each angular bin is proportional to the area of the wedge. (top) Results from the shallowest instruments and (bottom) the deepest instruments. (c),(d) Deviation from isotropy in the azimuthal axis of propagation of internal waves shown in colors. The hashed regions indicate a confidence of less than 95%. In all plots 0° is due east.

comparable in magnitude to the other processes. Two different statistical estimates (mean and median) of the lee wave flux are presented. The mean is much larger than the median, indicating that a few large lee wave generation events contributed strongly to the flux estimate. A simple drag parameterization suggests that, in this area, as much dissipation could be occurring within the bottom boundary layer as within the rest of the water column below 566 m. There are several limitations to this comparison that deserve acknowledgment and will be discussed further in the next section. Nevertheless, it is clear that eddy–wave interactions play a leading-order role in the energy budget of the mooring deployment area.

4. Discussion

Energy transfer rates between the mesoscale eddy and internal wave fields were quantified using a 14-month time series of current meter and CTD observations from a mooring array in the Southern Ocean. Previous attempts at measuring the eddy–internal wave interaction took place in the moderately energetic Northwest Atlantic and Gulf of Mexico, and were limited to depths shallower than 1000 m. Our analysis covers a much greater range of depths (including relatively close to topography) in a highly energetic region of the global

ocean. Unsurprisingly, our estimates differ from previous ones in a number of interesting ways.

a. Vertical energy transfer

A key finding of our work, not seen in past studies, is that the net energy transfer is from internal waves to eddies. The transfer arises from the interaction of the entire wave spectrum with eddy vertical shear. The magnitude of this transfer is about twice as large as estimated previously in the northwest Atlantic (Polzin 2010). Large uncertainties exist in the magnitude of the vertical transfer, mainly due to the unquantifiable impact of horizontal advection on the vertical velocity estimate. Nevertheless, it is a significant result that deserves discussion.

1) THE UPPER 2000 M

The large negative energy transfers we observe in the upper ocean depend, in part, on the strong shear associated with the ACC. The Southern Ocean may be a special environment since the mesoscale flow is approximately equivalent barotropic, with vertical shear extending to depth (Phillips and Bindoff 2014). It is also a region of strong internal wave generation, both by atmospheric forcing (Rimac et al. 2013) and flow over topography (e.g., Nikurashin et al. 2014; Cusack et al. 2017). Numerical modeling of eddy–internal wave
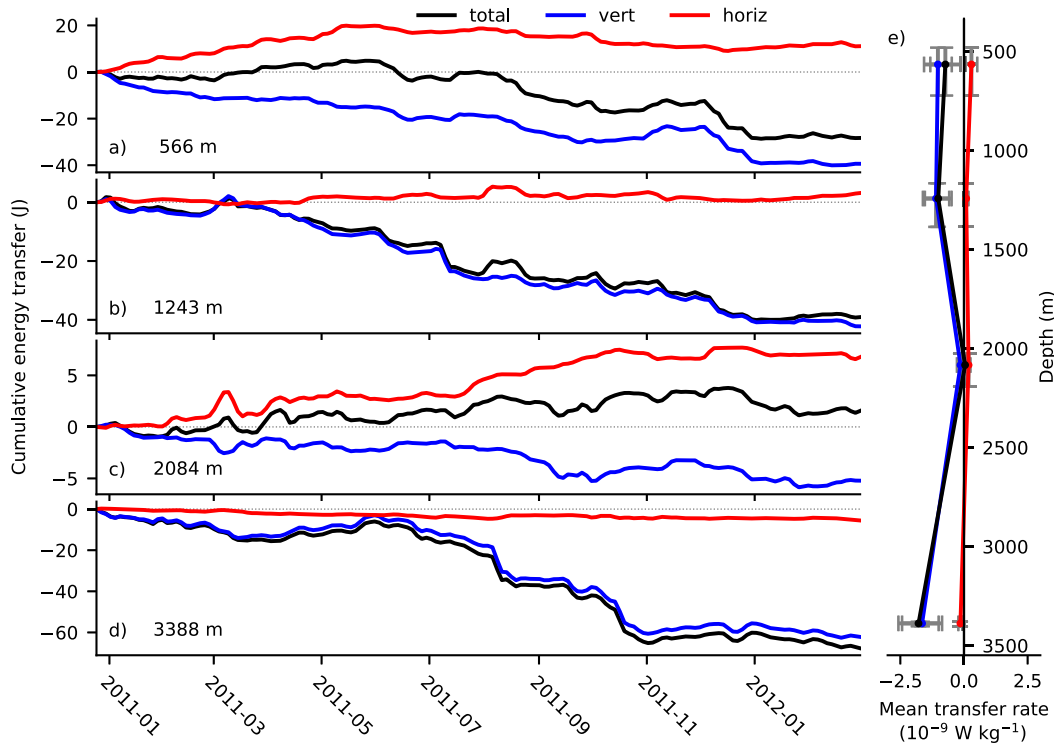
FIG. 12. Time series of cumulative energy transfer for the vertical, horizontal, and total terms from (a) 566, (b) 1243, (c) 2084, and (d) 3388 m, as well as (e) the time-mean transfer rate. Error bars represent the 95% confidence interval.

interactions in an ACC-like flow also shows a dominance of vertical transfer terms over horizontal, as well as the localization of energy transfer within jets (Shakespeare and Hogg 2018). Importantly, when the model waves are generated, they are preferentially oriented in the same horizontal direction as jets. Our observations do not suggest that the internal wave field is strongly anisotropic in the upper 2000 m; however,

this could be due to observational limitations. Past observations suggest the presence of vertical anisotropy, with a predominance of upward-propagating wave energy near the bottom typically associated with lee wave generation (Brearley et al. 2013; Sheen et al. 2013), although it is unclear whether this is the case for the upper 2000 m. There is an increase in the energy content of superinertial waves in the Scotia Sea
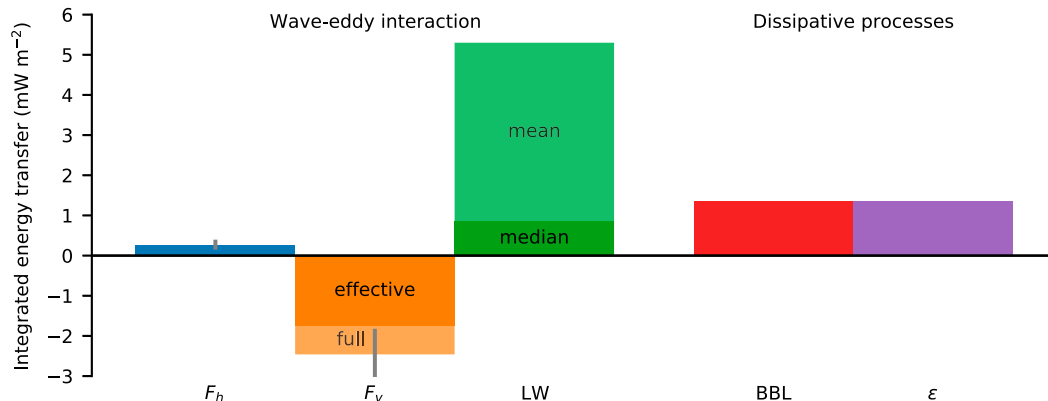

FIG. 13. Depth-integrated energy transfers and dissipative processes. The error bars, where they are available, represent the 95% confidence interval. The energy flux into lee waves (LW) is taken from (Brearley et al. 2013). Dissipative energy transfers include bottom boundary layer (BBL) drag, and measured depth-integrated turbulent dissipation rates from VMP data.

relative to the southeast Pacific (Sheen et al. 2013). It is possible that this additional high-frequency wave energy contributes to the vertical interaction.

2) THE LOWER 2000 m

To better understand how energy transfers of different sign may arise, it is illuminating to consider the transfer associated with the vertical propagation of a single plane wave through a parallel shear flow (e.g., Shakespeare and Hogg 2018). It can be shown that the sign of the transfer is equal to the sign of the product of horizontal wavenumber k, vertical wavenumber m, and shear $\partial \overline{u}/\partial z$. The wavenumber components represent the propagation direction of the wave in space. For example, a wave propagating westward ($k < 0$) and upward ($m < 0$) into negative shear ($\partial \overline{u}/\partial z < 0$) would be expected to lose energy to the mean flow. This is analogous to the situation observed near the Kerguelen Plateau, where upward-propagating lee waves are conjectured to encounter a critical layer (Waterman et al. 2014). Kunze and Lien (2019) suggest that the observed mismatch between lee wave energy fluxes and depth-integrated turbulent dissipation near the seafloor could be partly explained by the loss of wave energy to the mesoscale flow.

We also observe that waves lose energy to eddies near the bottom; however, shear is usually positive. For $\partial \overline{u}/\partial z > 0$, a negative transfer is possible if waves travel eastward ($k > 0$) and upward ($m < 0$). Using ADCP measurements from the same mooring array, Brearley et al. (2013) documented upward-propagating internal waves, consistent with bottom generation. Moreover, times of stronger internal wave shear variance, a precursor of turbulent mixing, were coincident with times of enhanced near-bottom eddy flow speed. We find that near bottom velocities are predominantly southwestward. The observed loss of wave energy would then be consistent with northeastward-orientated lee waves propagating upward into backing shear. However, it is unlikely that quasi-steady lee waves are picked up by our analysis, which is conducted in a stationary reference frame. The picture is complicated by internal tides, which we find to have a large amplitude near the bottom. Moreover, waves appear to be orientated predominantly southeastward, across the minor axis of the seamount, rather than northeastward. Even if a simple conceptual understanding of the processes occurring in the lower 2000 m remains elusive, it seems that flow–topography interactions play an important role.

The linearity of flow–topography interactions can be assessed with the steepness parameter, $s = hN/U$, where h represents the topographic height scale (e.g., Nikurashin et al. 2014). Nonlinear dynamics, including flow separation and blocking, are expected for $s > 0.4$. Our study area is characterized by a topographic height scale of ~500 m and near-bottom stratification of 10^{-3} rad s^{-1}, such that s will be greater than 0.4 for $U < 1.25$ m s^{-1}. Since the observed near-bottom flow is always weaker than this value, we expect nonlinear effects to be the norm. Thus, while we do not know what physical process induces the near-bottom horizontal buoyancy fluxes that underpin the bulk of our estimated eddy–internal wave energy transfer, it is unlikely that the process conforms to linear dynamics. It is possible that the physical assumptions of quasigeostrophy and linear internal waves underlying our analysis do not hold close to topography. More dedicated numerical modeling work and in situ observations will be required to untangle these dynamics.

b. Horizontal energy transfer

One similarity between our work and previous findings is that the horizontal energy transfer is significantly facilitated by straining of low-frequency waves ($<2f$) in the upper ocean. The sign of our estimate of the horizontal transfer rate is positive, indicating a transfer of energy from the mesoscale flow to internal waves. It is of the same sign and a similar magnitude to that found from the LDE array (Polzin 2010), and almost an order of magnitude greater than that diagnosed in the Gulf of Mexico (Jing et al. 2018). It is likely that we have underestimated the integrated horizontal transfer rate, since our observations do not extend to depths shallower than 500 m where the flux is expected to be positive (Jing et al. 2018) and eddy strain rates are greatest. For comparison with previous studies, we calculate the horizontal viscosity (see appendix A) and find it to be ~6 m^2 s^{-1}. This value is significantly smaller than that of Polzin (2010), which has formed the basis of global energy transfer estimates (Ferrari and Wunsch 2009). Our results would suggest that more work is required to understand the spatial variability in eddy–internal wave interaction before reliable global estimates can be made.

Our analysis is conducted in an Eulerian reference frame that is stationary with respect to the Earth. Idealized theoretical works on near-inertial wave–eddy interactions often rely on a generalized Lagrangian mean decomposition of the flow (Xie and Vanneste 2015; Rocha et al. 2018). The connection between these two viewpoints is subtle and may involve the "Stokes energy" [see Rocha et al. (2018) for a discussion]. We neglect these potential subtleties due to observational necessity. Broadly speaking, however, our results are consistent with theoretical and modeling papers suggesting that the horizontal straining component of eddy–near-inertial wave interactions extract energy from the

eddy field (e.g., Xie and Vanneste 2015; Taylor and Straub 2016; Rocha et al. 2018).

c. Horizontal divergence

The mooring array is located on a small seamount, on which significant flow–topography interactions have been identified in previous publications. Sévellec et al. (2015) showed that the characteristics of the time-mean meso-scale flow around the seamount are consistent with stratified Taylor column dynamics in the deepest 1000 m. There is also a time-mean QG vertical velocity, associated with time-mean horizontal convergence around the seamount.

If horizontal divergence is nonnegligible, as implied by Sévellec et al. (2015), then it may be necessary to retain additional terms that were previously neglected from the energy transfer equations. We cannot calculate the horizontal divergence accurately using the mooring array and must resort to order-of-magnitude estimates. The most significant additional term would involve the horizontal divergence of the time-mean flow multiplied by the internal wave energy density, i.e., $(u'^2 + v'^2)(\partial\overline{u}/\partial x + \partial\overline{v}/\partial y)$. Conceptually, an energy transfer is induced by isotropic squeezing of the internal wave field. To gauge the likely magnitude of this additional term, we estimate the horizontal divergence from values presented in Sévellec et al. (2015). Specifically, we take the time-mean vertical velocity to be $W \sim 10^{-3}$ m s^{-1}, and the rough vertical scale over which this velocity changes as $L \sim 1000$ m, giving a horizontal divergence similar to $W/L \sim 10^{-6}$ s^{-1}. Using high-pass-filtered velocity measurements from the mooring we estimate that the internal wave energy density is $\sim 10^{-3}$ J kg^{-1}. Thus, the order of magnitude of the additional term could be as large as 10^{-9} W kg^{-1}, which is similar to our estimates of horizontal and vertical energy transfer rates.

5. Conclusions

At the location of the DIMES mooring array, eddy–internal wave interactions play a leading-order role in the eddy and internal wave energy budgets. Their magnitude is a significant fraction of the time-mean wind work on the QG ocean circulation, despite the fact that observations miss the uppermost 500 m of the water column. Notably, the interactions act to energize eddies rather than dampen them. This result is partly a consequence of the energetic and deep-reaching shear of eddy flows in the Southern Ocean, and may also be related to anisotropy in the horizontal or vertical directions of internal wave propagation. Further research is needed to understand the energy transfers effected by buoyancy fluxes near topography. Given the global influence of Southern Ocean

eddy energetics (Marshall et al. 2017), establishing the wider representativeness of our local area-based findings stands out as an important future challenge.

APPENDIX A

Viscosity Parameterization

Müller (1976) derives the following equation describing the rate of change of total energy in the internal wave field:

$$\left(\frac{\partial}{\partial t} + \overline{\mathbf{u}} \cdot \nabla\right)E + \nabla \cdot \overline{\phi'\mathbf{u'}} = -\frac{1}{2}(\overline{u'u'} - \overline{v'v'})S_n - \overline{u'v'}S_s,$$

$$-(\overline{u'w'} - fN^{-2}\overline{b'v'})\frac{\partial\overline{u}}{\partial z}$$

$$-(\overline{v'w'} + fN^{-2}\overline{b'u'})\frac{\partial\overline{v}}{\partial z},$$

$$\text{(A1)}$$

where E represents the sum of internal wave kinetic and potential energy,

$$E = \frac{1}{2}(\overline{u'u'} + \overline{v'v'} + \overline{w'w'} + N^{-2}\overline{b'b'}), \qquad \text{(A2)}$$

and ϕ' is the wave pressure perturbation divided by density; u, v, w, and b denote zonal, meridional, and vertical velocity components and buoyancy, respectively. The normal and shear rate of strain are $S_n = \partial\overline{u}/\partial x - \partial\overline{v}/\partial y$ and $S_s = \partial\overline{v}/\partial x + \partial\overline{u}/\partial y$, respectively.

Previous papers ([Frankignoul 1976](); [Frankignoul and Joyce 1979](); [Ruddick and Joyce 1979](); [Brown and Owens 1981](); [Polzin 2010]()) parameterized the energy transfer using horizontal ν_h and vertical ν_v viscosity coefficients and a buoyancy diffusivity K_h given by the relations

$$-2\overline{u'v'} = \nu_h S_s, \tag{A3}$$

$$\overline{u'u'} - \overline{v'v'} = \nu_h S_n, \tag{A4}$$

$$\overline{u'w'} - \frac{f}{N^2}\overline{b'v'} = -\left(\nu_v + \frac{f^2}{N^2}K_h\right)\frac{\partial\overline{u}}{\partial z}, \tag{A5}$$

$$\overline{v'w'} + \frac{f}{N^2}\overline{b'u'} = -\left(\nu_v + \frac{f^2}{N^2}K_h\right)\frac{\partial\overline{v}}{\partial z}, \tag{A6}$$

where $\nu_v + f^2 K_h/N^2$ is the effective vertical viscosity from the combined action of vertical stresses and buoyancy fluxes. Substituting these back into Eq. [(A1)]() leads to

$$\left(\frac{\partial}{\partial t} + \overline{\mathbf{u}}\cdot\nabla\right)E + \nabla\cdot\overline{\phi'\mathbf{u'}} = \frac{1}{2}\nu_h(S_n^2 + S_s^2) + \left(\nu_v + \frac{f^2}{N^2}K_h\right)$$
$$\times\left[\left(\frac{\partial\overline{u}}{\partial z}\right)^2 + \left(\frac{\partial\overline{v}}{\partial z}\right)^2\right], \tag{A7}$$

whereby the energy transfer rate is proportional to the variance in eddy strain and shear. Note that Eq. [(A7)]() is different from that in [Polzin []()2010, their Eq. [(8)]()] by an amount $-(1/2)\nu_h\zeta^2$, where $\zeta = \partial\overline{v}/\partial x - \partial\overline{u}/\partial y$ is the vertical component of the relative vorticity. Applying Eq. [(A7)]() to our observations of energy transfer rate, shear variance and strain variance at 566-m depth gives $\nu_h = 6\,\mathrm{m^2\,s^{-1}}$ and $\nu_v + f^2 K_h/N^2 = -0.03\,\mathrm{m^2\,s^{-1}}$.

APPENDIX B

Error Quantification

Several sources of error are present in the final energy transfer estimates. In this section, we quantify the magnitude of each source of error and its impact on the final result.

a. Instrumental noise

Random noise is inherent to observational measurements. The power spectral density of velocity at the Nyquist frequency was found to match white noise with a standard deviation of $\sim 0.005\,\mathrm{m\,s^{-1}}$ for the Seaguard current meters, and $\sim 0.01\,\mathrm{m\,s^{-1}}$ for the Nortek current meters. The accuracy of the SBE37 temperature sensor is 0.002°C and that of the conductivity sensor is $0.0003\,\mathrm{S\,m^{-1}}$, which combine to an uncertainty in density

of approximately $1 \times 10^{-3}\,\mathrm{kg\,m^{-3}}$. Instrumental noise is not important in the eddy estimates, since they are averaged over $n = 512$ data points and the error on the mean scales as $1/\sqrt{n}$. The internal wave stresses may be more sensitive to noise; this will be assessed using a bootstrap procedure.

b. Interpolation error

Estimation of spatial gradients in eddy quantities requires that observations at the more sparsely instrumented outer moorings be interpolated or extrapolated to fixed height levels. The difference between the interpolated value and the true value at the fixed level is unknowable, and constitutes a source of error. To assess the likely magnitude of the error, we construct a virtual mooring in a regional numerical model of the real mooring location, and perform a motion correction identical to that applied to the observations. We then compare the strain and shear estimates from the virtual mooring with the "true" model value. The quality of the interpolated virtual mooring estimate is quantified by calculating the signal-to-noise ratio (SNR), equal to the variance of the virtual mooring estimate divided by the variance of the error. The key assumption is that the same signal to noise ratios apply in the observations, and can be used to derive an estimate of the real-world error. A more extensive examination of eddy–internal wave interactions in the model will be the subject of a future publication, and the model is only used in this paper to quantify error caused by observational sampling strategy.

We use MITgcm ([Marshall et al. 1997]()) to solve the 3D hydrostatic primitive equations in a domain extending from 75°–40°W to 52°–60°S with a horizontal grid spacing of 3.5 km and a variable vertical grid spacing of 8 m near the surface, tapering to 32 m at depth. It has a high-resolution region in the center of the domain with 700 m horizontal grid spacing. The model is centered on the real mooring array location for the time period 6 December 2010–21 November 2011, with a spinup period from 12 December 2009 to 5 December 2010. Bathymetry is taken from the GEBCO 2014 SID Grid version 20150318 ([Weatherall et al. 2015]()) with high-resolution multibeam data from DIMES cruises integrated around the mooring locations. The model is forced at the lateral boundaries with daily climatological values of velocity, temperature, and salinity from the GLORYS12V1 dataset (E.U. Copernicus Marine Service Information, https://marine.copernicus.eu/). The model is forced at the surface with hourly winds, precipitation, evaporation, and radiative and sensible heat fluxes from the ERA5 reanalysis ([Hersbach et al. 2020]()). In addition, the model is tidally forced by a tidal potential and boundary velocities derived from TPOX8 atlas 30c
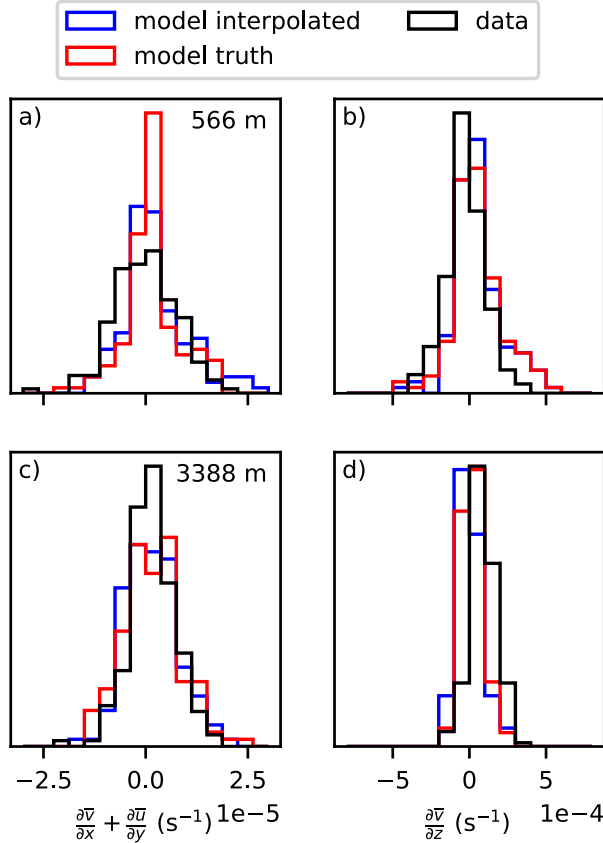
FIG. B1. Histograms of shear strain rate at (a) 566 and (c) 3388 m, as well as the meridional component of vertical shear at (b) 566 and (d) 3388 m, from observations, interpolated model output, and the true model output.

TABLE B1. Signal to noise ratios for velocity gradient estimates diagnosed from the model.

Depth (m)	$\dfrac{\partial \overline{v}}{\partial x} + \dfrac{\partial \overline{u}}{\partial y}$	$\dfrac{\partial \overline{u}}{\partial x} - \dfrac{\partial \overline{v}}{\partial y}$	$\dfrac{\partial \overline{u}}{\partial z}$	$\dfrac{\partial \overline{v}}{\partial z}$	$\dfrac{\partial \overline{u}}{\partial x} + \dfrac{\partial \overline{v}}{\partial y}$
566	5	3	27	21	1
1243	25	20	11	13	1
2084	6	7	13	17	1
3388	18	10	2	2	1

used in the energy transfer equations are reported in Table B1. We find that the SNR of the strain rate is lowest at 566 and 2084 m, and higher elsewhere. We also find that the SNR of the shear is low near the bottom. The SNR of the divergence is very low at all depths. This provides an additional pragmatic justification for assuming the mean flow to be QG, since noise in the divergence estimate would contaminate results from the full unapproximated energy equation.

c. Error in the horizontal derivatives

Spatial derivatives of eddy velocity rely on approximate numerical methods. Bryden and Fofonoff (1977) estimate the error in the horizontal derivatives by assuming that the mesoscale flow can be represented locally by a plane wave, $\overline{u} = \overline{u}_0 e^{i\mathbf{k}\cdot\mathbf{x}}$, with a dominant wave vector $\mathbf{k}$. The ratio of the estimated gradient to the true gradient in this case is given by

$$\frac{\sin\left(\dfrac{1}{2}\mathbf{k}\cdot\Delta\mathbf{x}\right)}{\dfrac{1}{2}\mathbf{k}\cdot\Delta\mathbf{x}}, \tag{B1}$$

where $\Delta\mathbf{x}$ is the spacing between the moorings. The error in the estimate for an eddy with a wavelength of 50 km, aligned with moorings spaced 10 km apart, is about 6%. This value represents a worst case scenario because most eddies at the latitude of the moorings have a larger wavelength (Chelton et al. 2011). We sum this error with the interpolation error, assuming independence, using standard error propagation methods (Taylor 1997).

d. Internal wave stress error

The internal wave stresses are estimated as the covariance of internal wave fluctuations in quantities that are subject to instrumental noise and interpolation error. We assume that noise and interpolation errors are random (not systematic), and proceed to estimate the error on the covariance with a bootstrap method. For each 512-point window, we bandpass filter the velocity and buoyancy time series between f and N, and build an empirical probability distribution of the covariance by recalculating the covariance 1000 times using random

data from the Tidal Model Driver (TMD) (Egbert and Erofeeva 2002).

The virtual mooring array is constructed by extracting depth–time slices from the model output at the location of the real moorings. We then subsample these slices at the real instrument minimum depths, plus an amount of knock-down Δz, which we take to be proportional to the cube of the instrument-average speed, in approximate agreement with the observational knock-down. The goal is not to perfectly reproduce mooring dynamics, but to provide a sufficiently realistic virtual mooring that can be used to assess the error introduced by interpolating sparse observations.

For the SNR diagnosed from the model to hold in reality, the velocity gradients in the model must be similar to those in the real world. Figure B1 compares shear strain rate and vertical shear between the interpolated model output, the model truth, and the real observations for two depths. The histograms are similar in shape, providing confidence that SNR can be applied to the real data. The SNR for the velocity gradients

TABLE B2. Signal to noise ratios for stress estimates diagnosed from bootstrapping.

Depth (m)	$\overline{u'v'}$	$\overline{u'u'} - \overline{v'v'}$	$\overline{u'w'}$	$\overline{v'w'}$	$\overline{u'b'}$	$\overline{v'b'}$
566	14	14	4	4	62	61
1243	15	15	4	4	73	66
2084	21	25	7	7	57	56
3388	11	22	17	24	97	67

resampling with replacement. We then take the variance of the distribution, which is found to approximate a normal distribution, as an estimate of the error. As with the eddy gradients, the quality of the stress estimates may be quantified using the signal to noise ratio. In this case, since each stress estimate is associated with its own error, we define the SNR as the mean error variance divided by the variance in stress over the full record. Table B2 lists the SNR values for each term in the energy transfer equation, for each mean depth level. We generally find a high SNR, with the exception of near-surface vertical stresses, where the SNR ~ 4.

e. Doppler shifting error

Advection of density gradients by the mean flow could lead to erroneous estimation of w' and the vertical stress. This can also be thought of as a Doppler shifting effect. Ruddick and Joyce (1979) provide a relationship between the true wave stress and the measured stress,

$$\overline{u'w'}_{\text{measured}} = \overline{u'w'}_{\text{true}} \Big/ \left(1 - \frac{\mathbf{k}_h \cdot \overline{\mathbf{u}}}{\omega_0}\right) \qquad \text{(B2)}$$

where $\mathbf{k}_h = (k, l)$ is the horizontal wavenumber. The correction goes as $\mathscr{O}(|\overline{\mathbf{u}}|/c_p)$, where c_p is the wave horizontal phase speed. High-frequency low-wavenumber waves have the greatest phase speed, since $c_p = \omega_0/|\mathbf{k}_h|$. If the internal wave field is comprised mostly of waves with a phase speed significantly greater than the eddy speed, then the measured estimate should be close to the true value. Internal waves oriented parallel to the eddy flow will be most strongly Doppler shifted, whereas those orientated perpendicular will be unaffected. It is not possible to estimate the phase speed, because we cannot determine the horizontal wavenumber components from our relatively sparse horizontal observations. Suspicion might be raised if stress is strongly correlated with eddy speed. However, we do not observe a correlation between eddy speed and vertical stress near the surface, where eddy flows are strongest. Near the bottom, there is some indication that stronger eddy speeds are associated with weaker stresses; however, eddy speeds are rarely greater than $0.1 \, \text{m s}^{-1}$. Throughout the water column, there is evidence that stronger flows are

associated with higher shear, which could have a more significant effect on the estimated energy transfer rate.

REFERENCES

Arbic, B. K., and Coauthors, 2009: Estimates of bottom flows and bottom boundary layer dissipation of the oceanic general circulation from global high-resolution models. *J. Geophys. Res.*, **114**, C02024, https://doi.org/10.1029/2008JC005072.

Bell, T. H., 1975: Lee waves in stratified flows with simple harmonic time dependence. *J. Fluid Mech.*, **67**, 705–722, https://doi.org/10.1017/S0022112075000560.

Booker, J. R., and F. P. Bretherton, 1967: The critical layer for internal gravity waves in a shear flow. *J. Fluid Mech.*, **27**, 513–539, https://doi.org/10.1017/S0022112067000515.

Brearley, J. A., K. L. Sheen, A. C. Naveira Garabato, D. Smeed, and S. Waterman, 2013: Eddy-induced modulation of turbulent dissipation over rough topography in the Southern Ocean. *J. Phys. Oceanogr.*, **43**, 2288–2308, https://doi.org/10.1175/JPO-D-12-0222.1.

Brown, E. D., and W. B. Owens, 1981: Observations of the horizontal interactions between the internal wave field and the mesoscale flow. *J. Phys. Oceanogr.*, **11**, 1474–1480, https://doi.org/10.1175/1520-0485(1981)011%3C1474:OOTHIB%3E2.0.CO;2.

Bryden, H. L., and N. P. Fofonoff, 1977: Horizontal divergence and vorticity estimates from velocity and temperature measurements in the MODE region. *J. Phys. Oceanogr.*, **7**, 329–337, https://doi.org/10.1175/1520-0485(1977)007%3C0329:HDAVEF%3E2.0.CO;2.

Bühler, O., and M. E. McIntyre, 2005: Wave capture and wave–vortex duality. *J. Fluid Mech.*, **534**, 67–95, https://doi.org/10.1017/S0022112005004374.

Cairns, J. L., and G. O. Williams, 1976: Internal wave observations from a midwater float, 2. *J. Geophys. Res.*, **81**, 1943–1950, https://doi.org/10.1029/JC081i012p01943.

Chelton, D. B., M. G. Schlax, and R. M. Samelson, 2011: Global observations of nonlinear mesoscale eddies. *Prog. Oceanogr.*, **91**, 167–216, https://doi.org/10.1016/j.pocean.2011.01.002.

Cronin, M., K. Tracey, and D. R. Watts, 1992: Mooring motion correction of the SYNOP Central Array current meter data. GSO Tech. Rep. 92-4, 114 pp.

Cusack, J. M., 2020: Jessecusack/DIMES_eddy_wave_interactions: Working upload of code and data. Zenodo, https://doi.org/10.5281/zenodo.3924818.

——, A. C. Naveira Garabato, D. A. Smeed, and J. B. Girton, 2017: Observation of a large lee wave in the Drake passage. *J. Phys. Oceanogr.*, **47**, 793–810, https://doi.org/10.1175/JPO-D-16-0153.1.

Dunphy, M., and K. G. Lamb, 2014: Focusing and vertical mode scattering of the first mode internal tide by mesoscale eddy interaction. *J. Geophys. Res. Oceans*, **119**, 523–536, https://doi.org/10.1002/2013JC009293.

Egbert, G. D., and S. Y. Erofeeva, 2002: Efficient inverse modeling of barotropic ocean tides. *J. Atmos. Oceanic Technol.*, **19**, 183–204, https://doi.org/10.1175/1520-0426(2002)019<0183:EIMOBO>2.0.CO;2.

Eliassen, A., and E. Palm, 1961: *On the Transfer of Energy in Stationary Mountain Waves.* I kommisjon hos Aschehoug, 23 pp.

Ferrari, R., and C. Wunsch, 2009: Ocean circulation kinetic energy: Reservoirs, sources, and sinks. *Annu. Rev. Fluid Mech.*, **41**, 253–282, https://doi.org/10.1146/annurev.fluid.40.111406.102139.

Frankignoul, C., 1976: Observed interaction between oceanic internal waves and mesoscale eddies. *Deep-Sea Res. Oceanogr. Abstr.*, **23**, 805–820, https://doi.org/10.1016/0011-7471(76)90848-2.

——, and T. M. Joyce, 1979: On the internal wave variability during the Internal Wave Experiment (IWEX). *J. Geophys. Res.*, **84**, 769, https://doi.org/10.1029/JC084iC02p00769.

Gonella, J., 1972: A rotary-component method for analysing meteorological and oceanographic vector time series. *Deep-Sea Res. Oceanogr. Abstr.*, **19**, 833–846, https://doi.org/10.1016/0011-7471(72)90002-2.

Hersbach, H., and Coauthors, 2020: The ERA5 global reanalysis. *Quart. J. Roy. Meteor. Soc.*, **146**, 1999–2049, https://doi.org/10.1002/qj.3803.

Hogg, N. G., 1986: On the correction of temperature and velocity time series for mooring motion. *J. Atmos. Oceanic Technol.*, **3**, 204–214, https://doi.org/10.1175/1520-0426(1986)003%3C0204:OTCOTA%3E2.0.CO;2.

——, 1991: Mooring motion corrections revisited. *J. Atmos. Oceanic Technol.*, **8**, 289–295, https://doi.org/10.1175/1520-0426(1991)008%3C0289:MMCR%3E2.0.CO;2.

Hughes, C. W., and C. Wilson, 2008: Wind work on the geostrophic ocean circulation: An observational study of the effect of small scales in the wind stress. *J. Geophys. Res.*, **113**, C02016, https://doi.org/10.1029/2007JC004371.

Jackett, D. R., and T. J. McDougall, 1997: A neutral density variable for the world's oceans. *J. Phys. Oceanogr.*, **27**, 237–263, https://doi.org/10.1175/1520-0485(1997)027%3C0237:ANDVFT%3E2.0.CO;2.

Jing, Z., P. Chang, S. F. DiMarco, and L. Wu, 2018: Observed energy exchange between low-frequency flows and internal waves in the Gulf of Mexico. *J. Phys. Oceanogr.*, **48**, 995–1008, https://doi.org/10.1175/JPO-D-17-0263.1.

Jones, W. L., 1969: Ray tracing for internal gravity waves. *J. Geophys. Res.*, **74**, 2028–2033, https://doi.org/10.1029/JB074i008p02028.

Kunze, E., 1985: Near-inertial wave propagation in geostrophic shear. *J. Phys. Oceanogr.*, **15**, 544–565, https://doi.org/10.1175/1520-0485(1985)015%3C0544:NIWPIG%3E2.0.CO;2.

——, and R.-C. Lien, 2019: Energy sinks for Lee waves in shear flow. *J. Phys. Oceanogr.*, **49**, 2851–2865, https://doi.org/10.1175/JPO-D-19-0052.1.

Lee, D.-K., and P. P. Niiler, 1998: The inertial chimney: The near-inertial energy drainage from the ocean surface to the deep layer. *J. Geophys. Res.*, **103**, 7579–7591, https://doi.org/10.1029/97JC03200.

Marshall, D. P., M. H. Ambaum, J. R. Maddison, D. R. Munday, and L. Novak, 2017: Eddy saturation and frictional control of the Antarctic circumpolar current. *Geophys. Res. Lett.*, **44**, 286–292, https://doi.org/10.1002/2016GL071702.

Marshall, J., and K. Speer, 2012: Closure of the meridional overturning circulation through Southern Ocean upwelling. *Nat. Geosci.*, **5**, 171–180, https://doi.org/10.1038/ngeo1391.

——, A. Adcroft, C. Hill, L. Perelman, and C. Heisey, 1997: A finite-volume, incompressible Navier Stokes model for studies of the ocean on parallel computers. *J. Geophys. Res.*, **102**, 5753–5766, https://doi.org/10.1029/96JC02775.

Molemaker, M. J., J. C. Mcwilliams, and X. Capet, 2010: Balanced and unbalanced routes to dissipation in an equilibrated Eady flow. *J. Fluid Mech.*, **654**, 35–63, https://doi.org/10.1017/S0022112009993272.

Müller, P., 1976: On the diffusion of momentum and mass by internal gravity waves. *J. Fluid Mech.*, **77**, 789–823, https://doi.org/10.1017/S0022112076002899.

Nikurashin, M., and R. Ferrari, 2011: Global energy conversion rate from geostrophic flows into internal lee waves in the deep ocean. *Geophys. Res. Lett.*, **38**, L08610, https://doi.org/10.1029/2011GL046576.

——, ——, N. Grisouard, and K. Polzin, 2014: The impact of finite-amplitude bottom topography on internal wave generation in the Southern Ocean. *J. Phys. Oceanogr.*, **44**, 2938–2950, https://doi.org/10.1175/JPO-D-13-0201.1.

Olbers, D. J., 1976: Nonlinear energy transfer and the energy balance of the internal wave field in the deep ocean. *J. Fluid Mech.*, **74**, 375–399, https://doi.org/10.1017/S0022112076001857.

Orsi, A. H., T. Whitworth, and W. D. Nowlin, 1995: On the meridional extent and fronts of the Antarctic circumpolar current. *Deep-Sea Res. I*, **42**, 641–673, https://doi.org/10.1016/0967-0637(95)00021-W.

Phillips, H. E., and S. R. Rintoul, 2000: Eddy variability and energetics from direct current measurements in the Antarctic circumpolar current south of Australia. *J. Phys. Oceanogr.*, **30**, 3050–3076, https://doi.org/10.1175/1520-0485(2000)030%3C3050:EVAEFD%3E2.0.CO;2.

——, and N. L. Bindoff, 2014: On the nonequivalent barotropic structure of the Antarctic circumpolar current: An observational perspective. *J. Geophys. Res. Oceans*, **119**, 5221–5243, https://doi.org/10.1002/2013JC009516.

Polzin, K. L., 2010: Mesoscale eddy–internal wave coupling. Part II: Energetics and results from PolyMode. *J. Phys. Oceanogr.*, **40**, 789–801, https://doi.org/10.1175/2009JPO4039.1.

Rimac, A., J. Storch, C. Eden, and H. Haak, 2013: The influence of high-resolution wind stress field on the power input to near-inertial motions in the ocean. *Geophys. Res. Lett.*, **40**, 4882–4886, https://doi.org/10.1002/grl.50929.

Rocha, C. B., G. L. Wagner, and W. R. Young, 2018: Stimulated generation: Extraction of energy from balanced flow by near-inertial waves. *J. Fluid Mech.*, **847**, 417–451, https://doi.org/10.1017/jfm.2018.308.

Ruddick, B. R., and T. M. Joyce, 1979: Observations of interaction between the internal wavefield and low-frequency flows in the north Atlantic. *J. Phys. Oceanogr.*, **9**, 498–517, https://doi.org/10.1175/1520-0485(1979)009%3C0498:OOIBTI%3E2.0.CO;2.

Scott, R. B., and Y. Xu, 2009: An update on the wind power input to the surface geostrophic flow of the World Ocean. *Deep-Sea Res. I*, **56**, 295–304, https://doi.org/10.1016/j.dsr.2008.09.010.

Sévellec, F., A. C. Naveira Garabato, J. A. Brearley, and K. L. Sheen, 2015: Vertical flow in the Southern Ocean estimated from individual moorings. *J. Phys. Oceanogr.*, **45**, 2209–2220, https://doi.org/10.1175/JPO-D-14-0065.1.

Shakespeare, C. J., and A. McC. Hogg, 2017: Spontaneous surface generation and interior amplification of internal waves in a regional-scale ocean model. *J. Phys. Oceanogr.*, **47**, 811–826, https://doi.org/10.1175/JPO-D-16-0188.1.

——, and ——, 2018: The life cycle of spontaneously generated internal waves. *J. Phys. Oceanogr.*, **48**, 343–359, https://doi.org/10.1175/JPO-D-17-0153.1.

Sheen, K., and Coauthors, 2013: Rates and mechanisms of turbulent dissipation and mixing in the Southern Ocean: Results from the Diapycnal and Isopycnal Mixing Experiment in the Southern Ocean (DIMES). *J. Geophys. Res. Oceans*, **118**, 2774–2792, https://doi.org/10.1002/jgrc.20217.

Sheen, K. L., and Coauthors, 2014: Eddy-induced variability in Southern Ocean abyssal mixing on climatic timescales. *Nat. Geosci.*, **7**, 577–582, https://doi.org/10.1038/NGEO2200.

Taylor, G. I., 1920: I. Tidal friction in the Irish Sea. *Philos. Trans. Roy. Soc. London*, **220**, 1–33, https://doi.org/10.1098/rsta.1920.0001.

Taylor, J. R., 1997: *An Introduction to Error Analysis: The Study of Uncertainties in Physical Measurements*. 2nd ed. University Science Books, 327 pp.

Taylor, S., and D. Straub, 2016: Forced near-inertial motion and dissipation of low-frequency kinetic energy in a wind-driven channel flow. *J. Phys. Oceanogr.*, **46**, 79–93, https://doi.org/10.1175/JPO-D-15-0060.1.

Trowbridge, J. H., and S. J. Lentz, 1998: Dynamics of the bottom boundary layer on the Northern California shelf. *J. Phys. Oceanogr.*, **28**, 2075–2093, https://doi.org/10.1175/1520-0485(1998)028<2075:DOTBBL>2.0.CO;2.

Waterman, S., K. L. Polzin, A. C. Naveira Garabato, K. L. Sheen, and A. Forryan, 2014: Suppression of internal wave breaking in the Antarctic circumpolar current near topography. *J. Phys. Oceanogr.*, **44**, 1466–1492, https://doi.org/10.1175/JPO-D-12-0154.1.

Weatherall, P., and Coauthors, 2015: A new digital bathymetric model of the world's oceans. *Earth Space Sci.*, **2**, 331–345, https://doi.org/10.1002/2015EA000107.

Whalen, C. B., J. A. MacKinnon, and L. D. Talley, 2018: Large-scale impacts of the mesoscale environment on mixing from wind-driven internal waves. *Nat. Geosci.*, **11**, 842–847, https://doi.org/10.1038/s41561-018-0213-6.

Wunsch, C., 1998: The work done by the wind on the oceanic general circulation. *J. Phys. Oceanogr.*, **28**, 2332–2340, https://doi.org/10.1175/1520-0485(1998)028%3C2332:TWDBTW%3E2.0.CO;2.

Xie, J. H., and J. Vanneste, 2015: A generalised-Lagrangian-mean model of the interactions between near-inertial waves and mean flow. *J. Fluid Mech.*, **774**, 143–169, https://doi.org/10.1017/JFM.2015.251.

Zhai, X., H. L. Johnson, and D. P. Marshall, 2010: Significant sink of ocean-eddy energy near western boundaries. *Nat. Geosci.*, **3**, 608–612, https://doi.org/10.1038/ngeo943.

Zhang, Z., J. Tian, B. Qiu, W. Zhao, P. Chang, D. Wu, and X. Wan, 2016: Observed 3D structure, generation, and dissipation of oceanic mesoscale eddies in the south China Sea. *Sci. Rep.*, **6**, 24349, https://doi.org/10.1038/srep24349.

——, B. Qiu, J. Tian, W. Zhao, and X. Huang, 2018: Latitude-dependent finescale turbulent shear generations in the Pacific tropical-extratropical upper ocean. *Nat. Commun.*, **9**, 4086, https://doi.org/10.1038/s41467-018-06260-8.